Available online at www.sciencedirect.com
ScienceDirect
Journal of Power Sources 160 (2006) 1425–1430
JOURNAL OF POWER SOURCES
www.elsevier.com/locate/jpowsour

A new electrode material for nickel–metal hydride batteries: MgNiPt alloy prepared by ball-milling

Elki C. Souza, J.F.R. de Castro, Edson A. Ticianelli *

Instituto de Química de São Carlos, USP, Av. do Trabalhador Sãocarlense 400, CP 780, CEP 13560-970, São Carlos, SP, Brazil

Received 18 January 2006; received in revised form 28 February 2006; accepted 1 March 2006
Available online 2 May 2006

Abstract

In this paper, the effects of platinum addition on the structure and electrochemical properties of MgNiPt (Pt = 1.0, 2.0 and 3.0 at.%) metal hydride alloys are discussed. The ternary alloys were processed by mechanical alloying and had their structures characterized by X-ray diffraction, transmission electron microscopy and in situ X-ray absorption spectroscopy. It is observed that the structure of the alloys is formed by amorphous and nanocrystalline phases, with the size of the nano-grains close to 5 nm. The electrochemical properties were evaluated by galvanostatic charge and discharge cycles using different discharge rates in the range of 10–80 mA g^{-1}. The best result was obtained for the $Mg_{49.0}Ni_{49.0}Pt_{2.0}$ alloy, which showed smaller decay of the discharge capacity as a function of the charge/discharge cycle number, retaining 64% of its initial discharge capacity (364 mAh g^{-1}) after 10 cycles.

Keywords: MgNiPt amorphous alloy; Electrode material; Element substitution; Discharge capacity; Cycle life; Ball-milling

1. Introduction

In the last years, several studies have demonstrated that magnesium-based alloys, particularly nanocrystalline and amorphous $Mg_{50}Ni_{50}$-based alloys prepared by mechanical alloying (MA), are promising materials for applications in the metal hydride (MH) electrode of Ni–MH batteries [1–4] because of the larger initial discharge capacity (close to 500 mAh g^{-1} [5]) compared to that of $LaNi_5$-type alloys (300 mAh g^{-1}) used in commercial Ni–MH batteries. However, this property decreases very rapidly after the electrochemical cycling of the materials in alkaline electrolyte due to the growth of a $Mg(OH)_2$ layer on the particles surface, but the effect can be decreased after addition of other metals, such as transition metals, partially replacing Ni and/or Mg [5].

In recent papers, the addition of noble metals on Mg–Ni-based alloys processed by mechanical alloying has been also reported [6,7]. Ma et al. [6] showed the enhancement of the electrochemical properties of a Mg–Ni alloy when Pd is added as alloying element. The authors reported the effectiveness of Pd to diminish the degradation of the discharge capacity of the alloys, mainly for a $(MgNi)_{90}Pd_{10}$ alloy, and this effect was ascribed to a reduction of the $Mg(OH)_2$ formation [6]. Improvement of electrochemical properties of Mg–Ni–Pd alloys obtained by rapid solidification was also reported by Inoue and co-workers [7]. In this case, the investigated alloy had the following composition: Mg 67–Ni 23–Pd 10 (in at.%). The results have shown that the discharge capacities first decrease and then increase with the increase of the charge/discharge cycle number, in contrast to the large degradation observed for Mg–Ni-based amorphous alloys prepared by MA. Values of discharge capacities larger than 500 mAh g^{-1} at discharge current densities of 10 and 20 mA g^{-1} were reported.

In the present work, ternary Mg–Ni–Pt alloys were synthesized by mechanical alloying and had their electrochemical properties evaluated by galvanostatic cycles of charge and discharge. In these alloys, Pt was partially substituted for Ni and Mg in a binary $Mg_{50}Ni_{50}$ (in at.%), resulting in MgNiPt (Pt = 1.0, 2.0 and 3.0 at.%) alloys. The microstructure of the materials was characterized by X-ray diffraction (XRD) and transmission electron microscopy (TEM). The electronic features of the alloys were assessed by using X-ray absorption spectroscopy (XAS) in the X-ray absorption near edge structure (XANES) region. The investigation of these ternary alloys was motivated by the possibility of obtaining electrodes with improved properties and

* Corresponding author.
E-mail address: edsont@iqsc.usp.br (E.A. Ticianelli).

0378-7753/$ – see front matter © 2006 Elsevier B.V. All rights reserved.
doi:10.1016/j.jpowsour.2006.03.018

reduced amounts of the expensive Pt. The beneficial effect of this noble metal in reducing the degradation of metal hydride alloys has been demonstrated for $LaNi_5$-type materials [8,9]. However, so far no work had been devoted to study the Pt alloying effects on the physical and electrochemical properties of Mg–Ni-based metal hydride alloys.

2. Experimental

The $Mg_{50}Ni_{50}$ and MgNiPt (Pt = 1.0, 2.0 and 3.0 at.%) alloys were processed by mechanical alloying under Ar atmosphere using a SPEX 8000 mixer mill continuously for 6 h. Magnesium (chips, 20 mesh, 98%, Aldrich), nickel (powder, 325 mesh, 99.97%, Aldrich) and platinum (powder, 200 mesh, 99.99%, Johnson Mathey) were used as starting materials. The vial and the balls were made of stainless steel and the ball to powder weight ratio was 10:1.

The X-ray absorption spectroscopy experiments were performed on the XAS beam line at the Brazilian Synchrotron Light Laboratory (LNLS). The radiation was monochromatized using Si(1 1 1) single crystal. Three ionization chambers were present: incident (I_o), transmittance (I_T) and reference (I_R) detectors. The reference channel was primarily used for internal calibration of edge position, using a pure Ni foil. The measurements were carried out in the transmission mode at the Ni K-edge. Ex situ XANES measurements were made for the uncycled materials with the samples consisting of discs with 2 cm^2 of geometric area, prepared by pressing a mixture of 30 mg of the alloy powder with 40 mg of Teflonized carbon (30 wt.%).

The alloys were also characterized by X-ray diffraction (XRD) and TEM by using a Siemens D5005 diffractometer (Cu Kα radiation) and a Philips CM120 microscope, respectively.

Samples for the electrochemical tests were prepared by cold pressing a mixture of 100 mg of the alloy powder with 100 mg of a blend of carbon black (Vulcan XC-72R) powder with 33 wt.% of polytetrafluoroethylene (PTFE, Teflon T-30, E.I. DuPont®) binder in a Ni screen with an area of 2 cm^2. The electrochemical measurements were carried out in a three-electrodes cell, with a Pt counter electrode, an Hg/HgO reference electrode and 6.0 mol L^{-1} KOH electrolyte. The charging current density of the electrodes was 200 mA g^{-1} of active material and the discharging current densities were 10, 20, 40 and 80 mA g^{-1}. The cut-off potential for the discharge steps was −0.4 V (versus Hg/HgO, 6 mol L^{-1}).

3. Results and discussion

Fig. 1 shows the XRD patterns of the $Mg_{50}Ni_{50}$ and MgNiPt (Pt = 1.0, 2.0 and 3.0 at.%) alloys, for 2θ in the range of 30–85°. XRD analyses with a longer acquisition time per angular step were also carried out (inset in Fig. 1) for some of the samples, for 2θ in the range of 15–60°. As shown in Fig. 1, a broad band can be observed (at ca. 35–50°) for all alloys, indicating the presence of a predominant amorphous structure. These are superimposed by less broadened diffraction peaks (Fig. 1), showing that nanocrystalline phases are also present. These phases were identified as: Mg_2Ni, $MgNi_2$, Ni and Pt.

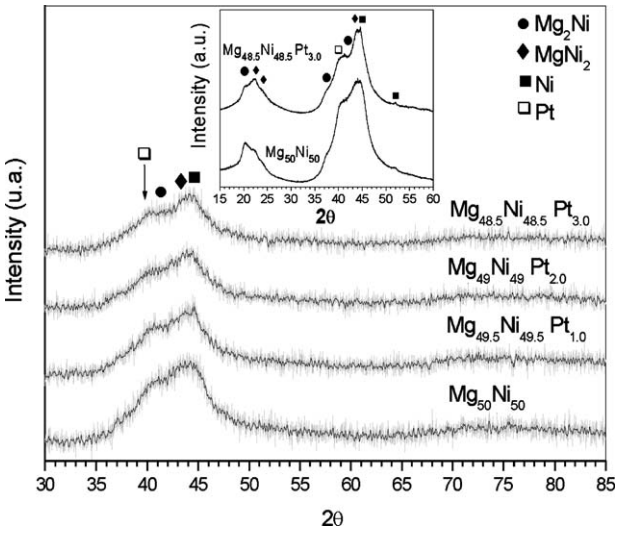

Fig. 1. X-ray diffraction patterns for the MgNi and MgNiPt (Pt = 1.0, 2.0 and 3.0 at.%) alloys.

Fig. 2 shows the TEM (a) bright-field and (b) dark-field images with the corresponding (c) selected area electron diffraction pattern (SAEDP) of the as-milled $Mg_{50}Ni_{50}$ alloy. The dark-field image (Fig. 2b) shows the nanostructure of the alloy, which evidences at the edge of the agglomerate the presence of particles with crystallite sizes of approximately 5 nm. The pattern of rings also indicates the nanometric grain size (Fig. 2c) of the alloy. Indexing the SAEDP's allowed the identification of the tetragonal Mg_2Ni (JCPDS 35-1225) phase.

Fig. 3 shows the TEM (a) bright-field and (b) dark-field images with the corresponding (c) SAEDP of the as-milled $Mg_{49.0}Ni_{49.0}Pt_{2.0}$ alloy. As in the previous case, also in this case the dark-field image and the pattern of rings (Fig. 3b and c) showed the nanostructure of the alloy with crystallite sizes of approximately 5 nm. Indexing the SAEDP's has evidenced the presence of the following phases: tetragonal Mg_2Ni (JCPDS 35–1225) and face centered cubic Pt (JCPDS 04-0802). Fig. 3c also indicates an overlapping between Pt and Mg_2Ni diffraction rings. Mg–Pt intermetallic phases were not observed and the solid solubility of Pt in Mg appears to be negligible, although it could be formed as indicated by its binary alloy phase diagram [10]. The partial replacement of Pt for Ni in the Ni-containing phases, during the formation of the alloy, is also possible since these elements can form solid solution at the amount of Pt utilized in present work [10]. Moreover, the incorporation of Pt into the amorphous phase can also occur. However, no evidences of such phenomena were apparent on the SAEDP results.

Normalized XANES spectra in the transmission mode at Ni K-edge for uncycled $Mg_{50}Ni_{50}$ and $Mg_{49.0}Ni_{49.0}Pt_{2.0}$ alloys and for the NiO and Ni foil standards are shown in Fig. 4. The absorptions at the Ni K-edge (Fig. 4) are due to excitations of 1s electrons to electronic states above the Fermi level [11,12]. Due to the selection rule, only transitions into empty p states are allowed. Weak quadrupole allowed 1s–3d transitions may be observed as small pre-edge peaks in the XANES [12] at ca. 0 eV. Theoretical calculations indicate that for distorted structures a mixing of p and d states can occur and, as a result, transitions

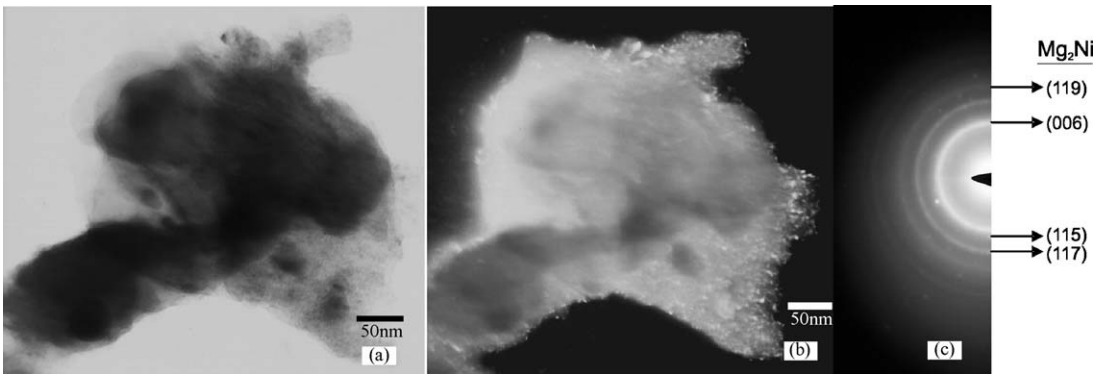

Fig. 2. TEM (a) bright-field and (b) dark-field images with the corresponding (c) SAEDP of the $Mg_{50}Ni_{50}$ alloy.

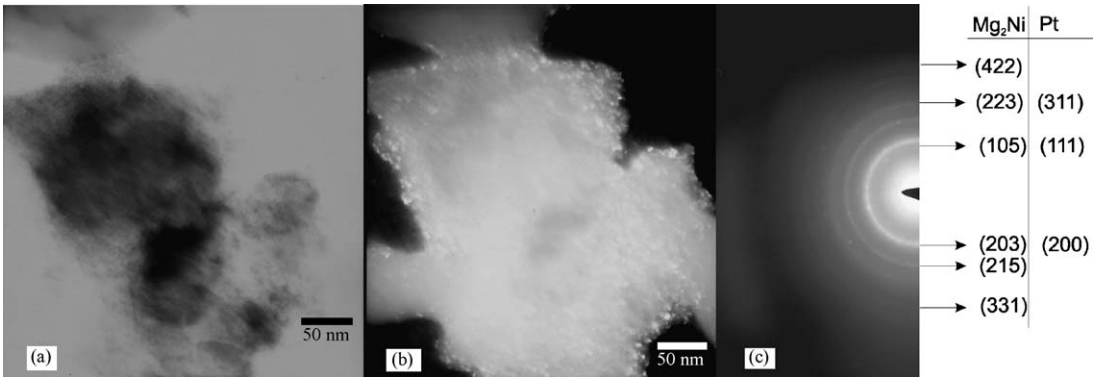

Fig. 3. TEM (a) bright-field and (b) dark-field images with the corresponding (c) SAEDP of the $Mg_{49.0}Ni_{49.0}Pt_{2.0}$ alloy.

into the empty p-like part of these mixed p–d states may take place [11–13], also explaining the presence of pre-edge peaks at ca. 0 eV. In Fig. 4 a large reduction of this feature is seen for NiO, in agreement with the large symmetry of the NiO cell as discussed in a previous publication [14]. On the contrary, for the $Mg_{50}Ni_{50}$ and $Mg_{49.0}Ni_{49.0}Pt_{2.0}$ alloys (Fig. 4) there is an appreciable increase of the pre-edge feature, consistent with the more disordered amorphous structure hosting the Ni atoms, as compared to the other two samples. It is also seen that the presence of Pt did not change the electronic properties of the Ni atoms and, by analogy, this may be also applied for Mg.

In Fig. 5 are the potential versus discharge capacity curves for the $Mg_{50}Ni_{50}$ and MgNiPt (Pt = 1.0, 2.0 and 3.0 at.%) alloys obtained during the first charge/discharge cycle. The curves in Fig. 5 displayed a single plateau during the discharge process, suggesting that a unique specie, i.e. hydrogen in hydride phases undergoes the electrochemical oxidation. However, it is possible

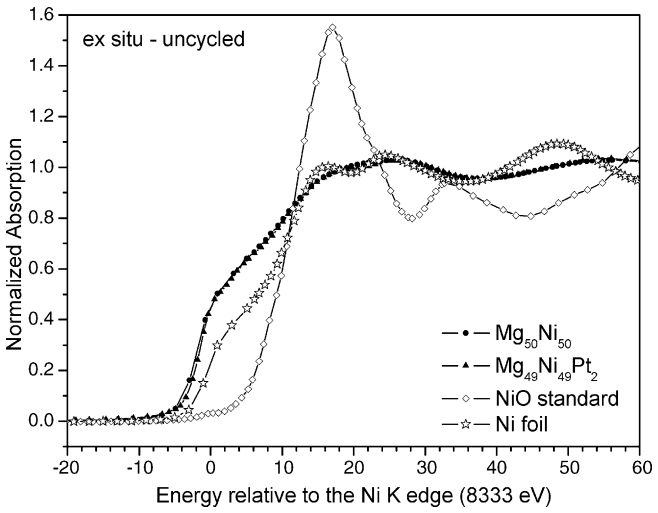

Fig. 4. XANES spectra in the transmission mode at the Ni K-edge for the uncycled $Mg_{50}Ni_{50}$ and $Mg_{49.0}Ni_{49.0}Pt_{2.0}$ alloys.

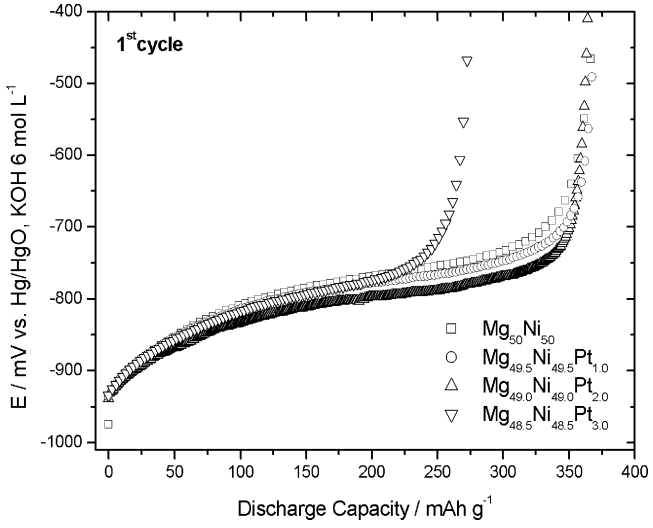

Fig. 5. Electrode potential vs. discharge capacity curves for the $Mg_{50}Ni_{50}$, MgNiPt (Pt = 1.0, 2.0 and 3.0 at.%) alloys at the first cycle of charge/discharge in discharging current density of 20 mA g^{-1}.

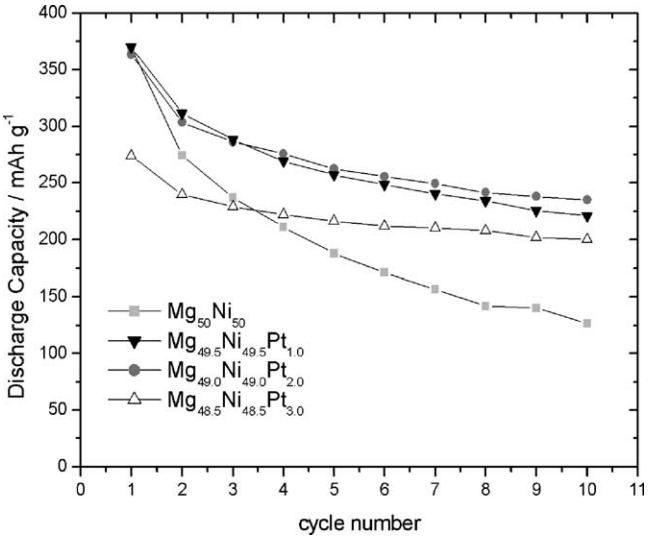

Fig. 6. Discharge capacity as a function of cycle number for the electrodes formed by Pt-containing Mg–Ni-based alloys.

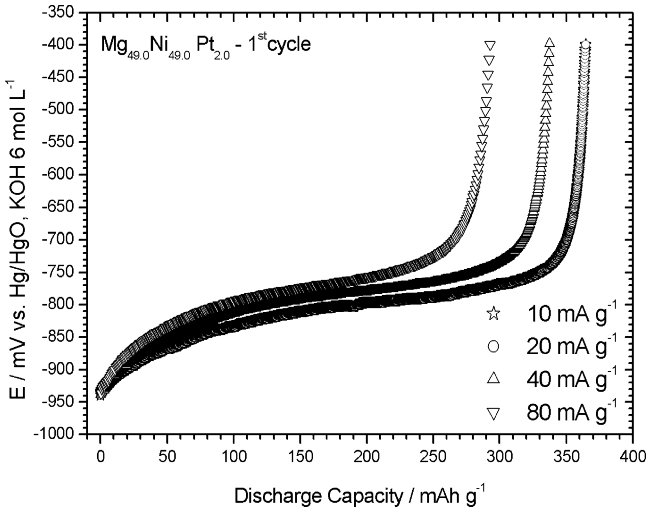

Fig. 7. Electrode potential vs. discharge capacity curves for $Mg_{49.0}Ni_{49.0}Pt_{2.0}$ alloy at the first cycle of charge/discharge at different discharge current densities (10, 20, 40 and 80 mA g^{-1}).

to observe that the plateaus are not flat. The slope of the plateaus is related to the presence of multiphases and/or to the partial amorphous structure of the alloy, which is more disordered (i.e. it does not present long range order) than the conventional polycrystalline systems. Consequently, there is a more broadened distribution of energy of the sites available for hydrogen occupation [15,16]. It is also observed that the presence of Pt did not appreciably change the values of the discharging potential at low discharging times, indicating little effect of Pt on the discharging reaction kinetics.

Fig. 6 shows plots of the total discharge capacity as a function of the charge/discharge cycle number for the $Mg_{50}Ni_{50}$ and MgNiPt (Pt = 1.0, 2.0 and 3.0 at.%) alloys. It is noted that the values of the discharge capacities are significantly dependent on the alloy composition. Comparing the results for $Mg_{50}Ni_{50}$, $Mg_{49.5}Ni_{49.5}Pt_{1.0}$ and $Mg_{49.0}Ni_{49.0}Pt_{2.0}$ it is observed that they present similar values of the initial discharge capacity (ca. 380 mAh g^{-1}), but the addition of Pt strongly affects the degradation rate of the electrode. For the alloy with a larger amount of Pt ($Mg_{48.5}Ni_{48.5}Pt_{3.0}$), the degradation kinetics of the electrodes was also retarded but this is accompanied by a decrease of the initial discharge capacity. Comparing the discharge capacities at the tenth charge/discharge cycle, it is noted that the MgNiPt alloys have similar values of discharge capacity (between 200 and 235 mAh g^{-1}) while for $Mg_{50}Ni_{50}$ the value is much smaller (128 mAh g^{-1}). After the fourth cycle, there is a clear tendency of the curves to reach a plateau, particularly for the Pt-containing materials, evidencing a large decrease of the alloy degradation with the progress of the electrode cycling.

Fig. 7 shows potential versus discharge capacity curves for the $Mg_{49.0}Ni_{49.0}Pt_{2.0}$ alloy at the first charge/discharge cycle, at different discharge current densities (10, 20, 40, 80 mA g^{-1}). These results show that the maximum discharge capacity generally decreases for increasing discharge currents, indicating that for low states of charge and high discharge currents the diffusion of hydrogen becomes the rate determining step of the dehydriding process and this drives to zero the hydrogen concentration in the alloy particle surface, while the core still contains a hydride phase. This effect is anticipated for high discharging rates implying that at the cut-off potential the amount of hydrogen remaining inside the particles is larger for higher discharging current densities. This phenomenon was confirmed by an experiment with the $Mg_{49.0}Ni_{49.0}Pt_{2.0}$ alloy, in which the discharge at a high current density (80 mA g^{-1}) was followed by a second discharge at a low current density (10 mA g^{-1}), as shown in Fig. 8. This experiment showed that the amount of hydride remained inside the alloy after discharging at 80 mA g^{-1} still represents ca. 70 mAh g^{-1}.

Table 1 shows values of discharge capacities for the first (C_1) and tenth (C_{10}) charge/discharge cycles, measured at different discharge current densities for the $Mg_{50}Ni_{50}$ and $Mg_{49.0}Ni_{49.0}Pt_{2.0}$ alloys. For both alloys it is observed that the

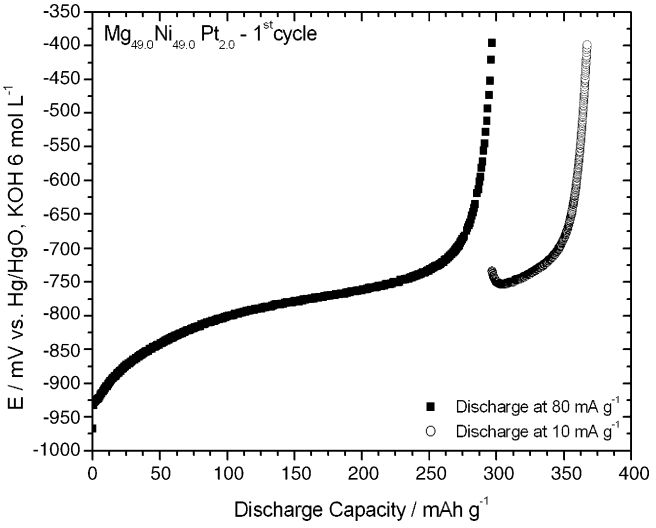

Fig. 8. Electrode potential vs. discharge capacity curves for the $Mg_{49.0}Ni_{49.0}Pt_{2.0}$ alloy first discharged at a high current density (80 mA g^{-1}) and the at low discharge current density (10 mA g^{-1}).

Table 1
Cycling dischargeability of the $Mg_{50}Ni_{50}$ and $Mg_{49.0}Ni_{49.0}Pt_{2.0}$ electrodes measured at different discharge current densities

Discharge current (mA g^{-1})	$Mg_{50}Ni_{50}$			$Mg_{49.0}Ni_{49.0}Pt_{2.0}$		
	C_1 (mAh g^{-1})	C_{10} (mAh g^{-1})	C_{10}/C_1	C_1 (mAh g^{-1})	C_{10} (mAh g^{-1})	C_{10}/C_1
10	363.93	100.40	0.27	364.28	218.18	0.60
20	369.26	126.42	0.34	363.50	234.84	0.64
40	300.46	89.36	0.30	324.59	187.37	0.57
80	236.36	73.60	0.31	292.87	137.40	0.47

C_1 and C_{10}: discharge capacities at the first and tenth cycles, respectively.

measured initial discharge capacities (C_1) and those at the 10th cycle (C_{10}) increase with the decrease of the discharge current density. The performance degradation for the $Mg_{49.0}Ni_{49.0}Pt_{2.0}$ alloy were attenuated drastically at all current densities compared to $Mg_{50}Ni_{50}$. Also, particularly in the case of the Pt-containing alloy, the C_{10}/C_1 ratios increase with the decrease of the discharging current densities down to 20 mA g^{-1}, after which the tendency is reversed. This result seems to indicate that the values of the discharge capacities are dependent of two factors: the rate of the hydrogen diffusion in hydride phase, as mentioned above, which raises the measured discharge capacity for low current densities and; the exposition time of the alloy to the electrolyte, which enhances the alloy corrosion, decreasing the discharge capacity when lower discharge current densities are employed. A compromise between these two opposite tendencies seems to be reached at a discharge current density of 20 mA g^{-1}.

Fig. 9 shows the XRD patterns for the $Mg_{50}Ni_{50}$ and $Mg_{48.5}Ni_{48.5}Pt_{3.0}$ alloys, after 10 charge/discharge cycles. As also shown for the uncycle alloys (Fig. 1) broad bands and broadened diffraction peaks are seen indicating that the predominant amorphous structure is maintained after cycling. The phases present after cycling were identified as: Mg_2Ni, $Mg(OH)_2$ and Pt. In the $Mg_{48.5}Ni_{48.5}Pt_{3.0}$ alloy the peak intensity of the nanocrystalline $MgNi_2$ phase is more intense than for the cycled

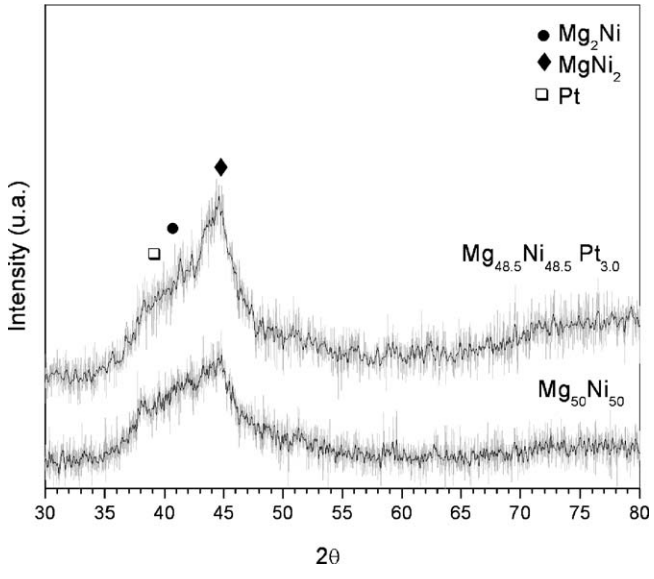

Fig. 9. X-ray diffraction patterns for the cycled $Mg_{50}Ni_{50}$ and $Mg_{48.5}Ni_{48.5}Pt_{3.0}$ alloys.

$Mg_{50}Ni_{50}$ and also for the uncycled $Mg_{48.5}Ni_{48.5}Pt_{3.0}$. This result may indicate that the presence of Pt induces a partial crystallization of some of the amorphous MgNi phase, when the alloy is subjected to repeated hydriding/dehydriding cycles.

Previous studies concerning the stability of Mg–Ni alloys in alkaline electrolyte reported that the formation of $Mg(OH)_2$ on the surface of the Mg–Ni particles during the electrochemical cycling plays a major role on the degradation of the discharge capacity of the electrodes [6]. This deleterious effect of the $Mg(OH)_2$ phase has been attributed to the reduction of the electron-transfer reaction rate, decreasing the overall rate of the hydrogen desorption [17]. The addition of other transition metal elements, such as Ti, Pd and Zr, among others, has been reported to improve into some extent the electrochemical stability of the Mg–Ni-based alloy electrodes [5–7,18]. When the properties of the Mg–Ni–Pt ternary alloys are compared to those of, for example, Mg–Ni–Ti alloys [5] with approximately the same Mg/Ni atomic ratio, it is noted that the initial discharge capacities for the Mg–Ni–Pt alloys are smaller than those for the Mg–Ni–Ti alloys. However, it is clearly observed that Pt is as effective as Ti for improving the electrode cycle life, as seen from the C_{10}/C_1 values. Results show that $Mg_{0.95}Ti_{0.05}Ni$ alloy retains 62% of its initial charge capacity after 10 cycles, while the $Mg_{49}Ni_{49}Pt_2$ alloy retains 64%.

In the case of Ti, the formation of a protective thin film of titanium oxide has been considered as responsible for the improvement of the electrode stability in alkaline medium [5]. These oxide films may retard the formation of the $Mg(OH)_2$ phase improving the lifetime of the electrode. In the present case, the improvement of the metal hydride alloy stability may be due to an enrichment of Pt on the Mg–Ni particle surface. Due to the high stability of metallic Pt in alkaline medium, the Pt-rich surface layer may act as a protective coat for the Mg in the bulk of the particle, retarding the formation of the $Mg(OH)_2$ phase.

4. Conclusions

XRD and TEM analyses revealed that the Mg–Ni–Pt alloys are composed by both, amorphous and nanocrystalline phases, with average crystallite sizes of approximately 5 nm. After 10 charge/discharge cycles, the predominant amorphous structure is maintained, but the peak intensity of the nanocrystalline Mg_2Ni phase is more intense than for cycled $Mg_{50}Ni_{50}$ or for uncycled Pt-containing materials. This result indicates that the presence of Pt induces some crystallization of an amorphous

MgNi phase, when the alloy is subjected to repeated hydriding/dehydriding cycles. The features of the XANES spectra at the Ni K-edge for the uncycled alloys were consistent to a disordered amorphous structure hosting the Ni atoms. It is also seen that the presence of Pt did not change the electronic properties of the Ni and eventually of the Mg atoms.

The data of the discharge capacities as a function of the cycle number, measured at different discharge current densities, indicate that the magnitude of the discharge capacities depend on two factors: the rate of the hydrogen diffusion in hydride phase which raises the discharge capacity for low current densities and; the exposition time of the alloy to the electrolyte, which enhances the alloy corrosion, decreasing the discharge capacity when low discharge current densities are employed.

In summary, considering both, the maximum discharge capacity and the cycle life, the best electrochemical performance was achieved with the $Mg_{49.5}Ni_{49.5}Pt_{2.0}$ alloy. This positive effect of Pt on the stability of the alloys may be associated to an enrichment of the particle surface with Pt, retarding the formation of $Mg(OH)_2$. Further research is under progress aiming to fully characterize the role of Pt on the improvement of the Mg–Ni cycling properties.

Acknowledgements

The authors wish to thanks FAPESP, CNPq and National Synchrotron Light Source (LNLS) in Brazil for financial support.

References

[1] L. Liao, W. Liu, X. Xiao, J. Electroanal. Chem. 566 (2004) 341–350.
[2] N. Cui, P. He, J.L. Luo, Electrochim. Acta 44 (1999) 3549–3558.
[3] J.-W. Liu, H.-T. Yuan, J.-S. Cao, Y.-J. Wang, J. Alloys Compd. 392 (2005) 300.
[4] C. Rongeat, L. Roué, J. Alloys Compd. 404–406 (2005) 679–681.
[5] S. Ruggeri, L. Roué, J. Huot, R. Schulz, L. Aymard, J.-M. Tarascon, J. Power Sources 112 (2002) 547–556.
[6] T. Ma, Y. Hatano, T. Abe, K. Watanabe, J. Alloys Compd. 372 (2004) 251.
[7] S.-I. Yamaura, H.-Y. Kim, H. Kimura, A. Inoue, Y. Arata, J. Alloys Compd. 347 (2002) 239.
[8] T.L. Markin, R.M. Dell, J. Electroanal. Chem. 118 (1981) 217.
[9] R.C. Ambrosio, E.A. Ticianelli, J. Solid State Eletrochem. 8 (2004) 532–537.
[10] T.B. Massalski, ASM/NIST Data Program for Alloy Phase Diagrams on CD-ROM, OH 44073, USA.
[11] B. Lengeler, R. Zeller, J. Less-Common Met. 103 (1984) 337.
[12] M. Gupta, J. Less-Common Met. 130 (1987) 219.
[13] D.A. Tryk, I.T. Bae, Y. Hu, S. Kim, M.R. Antonio, D.A. Scherson, J. Electrochem. Soc. 142 (1995) 824.
[14] H.-C. Huang, Y.-L. Wei, Y.-W. Yang, J.-F. Lee, J. Electron Spectrosc. Relat. Phenom. 144–147 (2005) 825.
[15] R. Kirchheim, F. Sommer, G. Schluckebier, Acta Metall. 30 (1982) 1059.
[16] Q.M. Yang, M. Ciureanu, D.H. Ryan, J.O. Strom-Olsen, J. Alloys Compd. 274 (1998) 266–273.
[17] Y. Hatano, T. Tachikawa, D. Mu, T. Abe, K. Watanabe, S. Morozumi, J. Alloys Compd. 330–332 (2002) 816.
[18] H.Y. Lee, N.H. Goo, W.T. Jeong, K.S. Lee, J. Alloys Compd. 313 (2000) 258–262.